11TH INTERNATIONAL MECHANICAL POWER ENGINEERING
CONFERENCE(IMPEC11),CAIRO, FEB(5-7), 2000

EXPERIMENTAL AND NUMERICAL INVESTIGATION OF FLOW CHARACTERISTICS IN A RECTANGULAR CHANNEL WITH TWO RIBBED-WALLS

A. S. Hanafi[1]; K. M. El-Shazly[2] and A. A. Abdel-Aziz[2]

Mechanical Eng. Dept., Zagazig University, Faculty of Engineering-Shoubra, Cairo, Egypt, Fax 202-2023336

ABSTRACT

The internal cooling passages of the turbine blades should be designed to yield the desired heat transfer augmentation with a minimum friction factor. The combined effect of rib pitch, rib geometry, and rib alignment on the friction factor and pressure distributions on rib surface for fully developed flow in a rectangular duct with two opposite ribbed-walls were determined for Reynolds numbers (based on the duct hydraulic diameter) ranging from 12,000 to 65,000. The duct aspect ratio is 4:1 and the rib pitch to height ratios were 10, 20, and 40; the rib height to duct hydraulic diameter ratio and duct height are kept at 0.081 and 0.125, respectively. Pressure taps are distributed over the bottom-ribbed wall and the rib itself to calculate the friction factor and static pressure coefficient distributions on the rib surface, respectively. ANSYS FLOTRAN CFD computer package was applied to predict the flow separation, recirculation, reattachment, and wake regions to support the experimental results from the flow visualization and the duct measurements. A comparison between the theoretical and experimental results and also with the previous results was investigated. Experimental correlations for the average static pressure coefficient on the rib surface and the friction factor are developed in terms of Reynolds number (Re) and rib pitch to height ratio (p/e) for fully developed flow in ribbed-channel with different rib shapes. The experimental correlations of the average static pressure coefficient on rib surface with different rib shapes are developed in terms of Reynolds number and rib pitch to height ratio. Also the friction factor correlations for different rib shapes are developed.

$$\overline{C_p} = a_1.\mathrm{Re}^{a_2}.(p/e)^{a_3} \quad (1)$$

$$f = b_1.\mathrm{Re}^{b_2}.(p/e)^{b_3} \quad (2)$$

The constant coefficients a_1, a_2, a_3, b_1, b_2, and b_3 are listed in table 2. The maximum relative errors in equation (1) are ± 6 %, ± 9 %, and ± 4 % for trapezoidal, square and inverted trapezoidal ribs, respectively, and in equation (2) are ± 9 %, and ± 12 % for trapezoidal and inverted trapezoidal ribs, respectively.

KEYWORDS: Flow through channel, Ribbed-walls, Rib geometry, Flow visualization, ANSYS CFD, Pressure measurements.

1. INTRODUCTION

Many experimental investigations have been conducted to determine the effect of geometric parameters of ribbed-ducts that produce optimum results in terms of heat

[1] Faculty of Engineering, Mech. Power Eng. Dept., Cairo University, Giza, EGYPT.

[2] Faculty of Engineering, Mech. Eng. Dept., Shoubra, Zagazig University, Cairo, EGYPT.

transfer and pressure drop. In the cooling passage of turbine blade, artificial turbulence promoters are installed on the two opposite walls of the internal cooling passage for heat transfer enhancement with minimum pumping power. Therefore, an optimal rib geometry is investigated experimentally and numerically to give an improvement in heat transfer coefficients for the same mass flow rate through the cooling passage. The relevant geometry parameters in previous work are the channel aspect ratio [Han, 1988 and Hong, et. al., 1993], rib angle orientation [Han, et. al., 1991], rib shape [Liou et. al., 1992 (part1)] (square, triangle, and semi-cylindrical rib shapes), rib spacing [Liou et. al., 1992 (part 2)], and blockage ratio [Han, 1984]. Up to the year (1991), the numerical simulation of turbulent flow through channel of one ribbed wall in the previous work is investigated for fixed rib geometry [Liou, et. al., 1993]. Therefore, in the present work ANSYS FLOTRAN CFD package [ANSYS, 1997] is used to determine numerically the hydrodynamic effect of rib geometry on the flow characteristics for forced convection through channel with two opposite roughened-walls. The static pressure distributions on the rib surface itself for fully developed flow through ribbed-duct is investigated experimentally and numerically. Table 1 shows briefly the rib shapes, rib pitches, and coordinate system used in the present study. Flow visualization results were carried out to support the measured results and illustrate the flow characteristics around the ribs.

TABLE 1: RIB GEOMETRY AND COORDINATE SYSTEM USED IN THE PRESENT EXPERIMENTAL WORK

Rib Geometry	H (mm)	e. (mm)	a. (mm)	p/e	θ	Shape
Square	40	5.2	5.2	10 20 40	90°	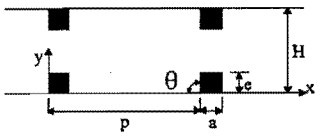
Trapezoidal	40	5.2	7	10 20 40	97°	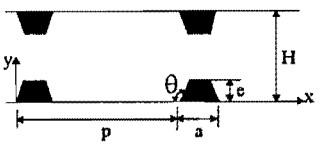
Inverted Trapezoidal	40	5.2	7	10 20 40	83°	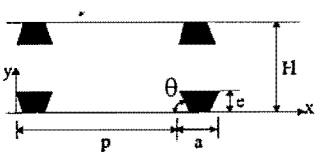

N.B. Test section has 46, 22, and 10 ribs at p/e =10, 20, and 40, respectively, Re =12,000 to 65,000, e/De = 0.081.

2. EXPERIMENTAL INVESTIGATION

Study of the flow characteristics through ribbed-duct was carried out in two channels. A special apparatus was built up for flow measurements, and a special simulated model was built up also, for flow visualization. The flow system consists of: air blower, orifice flow meter, transition duct, straightener, test section, main entrance duct, and bell mouth intake duct. The schematic diagram of the test rig is shown in Fig. 1. The air blower is of the centrifugal type. An AC coupled motor of 3 HP drives it. The airflow discharge is controlled at the outlet of the air blower by means of a variable area outlet gate.

2.1 Test Section

The main duct, which supplies air to the test section, is a horizontal rectangular duct having dimensions 160 mm × 40 mm, i.e. the duct aspect ratio of 4:1 is the same aspect ratio employed by Liou et. al., 1992 (part 2) for the studies of rib roughness channel flows. The duct is connected to the test section by means of flange and rubber sheets to avoid air leakage. The test section consists of two principle walls (the top and bottom walls of the duct) and two side walls were 1200 mm in length and had a rectangular cross-section 160 mm (aluminum plate) × 40 mm (plexiglas) (z-y plane) i.e., having aspect ratio of 4:1. Each principal wall was covered by full aluminum ribs of different shapes with a height of 5.2 mm and a length of 160 mm. The side-walls of the entire test section are made of Plexiglas plates (8 mm thick) to provide good view for spatial optical technique measurements. A digital Micro-Manometer is used to measure the differential pressure and air velocity. Six pressure taps were used for static pressure drop measurements across the fully developed regions of the test duct as shown in Fig. 2. The static pressure distributions on the rib surface are taken for the rib number 16 at x/De = 13.7, nine pressure taps at mid-span of rib where the hydrodynamic fully developed conditions are achieved. The pressure taps were drilled with a diameter of 0.25 mm at intervals of $(1/3)e$ (e is the rib height) for front and back faces of rib, and $(1/4)e$ for the upper face of rib as shown in Fig. 3. The calibration of the wind tunnel is made to check whether the airflow is uniform at entrance to the rib-roughened channel and a boundary layer probe checks the two-dimensionality of the spanwise velocity profile of the flow.

A check of two dimensionality of the airflow across the test section width is investigated by the spanwise distributions of the axial pressure with different values of Reynolds number followed a method developed by Liou and Chen, 1998. It is shown from Fig. 4

that the maximum scatter of the average pressure in spanwise direction is typically within 5 % of the duct spanwise average pressure.

In order to find the qualitative characteristics of the flow field around the ribs, a smoke visualization technique was employed in a smoke tunnel. The smoke tunnel is used to view flow patterns, recirculation, separation, and the reattachment point around the ribs at different speeds. Models are attached to the rear wall of the working section while the front wall is of Plexiglas and is readily movable. The smoke is driven upwards to the test section by a suction fan. In order to obtain the flow pattern characteristics from the smoke visualization process, a computer analysis technique is applied in the present work. A video camera is used to view and record the smoke-visualized flow pattern through the ribbed-duct with different rib pitches and shapes. The output video picture is seen on the computer's monitor, and then is captured using a special capture utility program. This system's unique advantage of variable slow-motion-playback, still framing and slow motion reverse playback allowed a detailed and clear picture of the flow pattern.

3. EXPERIMENTAL RESULTS

In the fully developed region, the flow patterns repeat themselves cyclically as shown before by Liou et. al., 1993 by using LDV technique. Therefore, the static pressure distributions on rib and the pressure drop through ribbed wall were measured in the fully developed region at $9 \leq x/De \leq 18$. Flow measurements were carried out through the ribbed-duct versus Reynolds numbers with different rib pitches, rib shapes, and types of rib alignment. All of these experiments have been carried out at same rib height (e/De = 0.081). The static pressure distribution was normalized by the fluid dynamic pressure in the form of pressure coefficient (C_p). The friction factor in the fully developed region was calculated from the pressure drop across the flow duct by pressure taps located at the bottom ribbed wall and mass flow rate of the air as follows:

$$f=\frac{(\Delta p/\Delta x)De}{2\rho U_m^{\,2}}, \qquad C_p=\frac{(p_s-p_\infty)}{0.5\rho U_m^{\,2}}, \qquad C_{p_b}=\frac{(p_b-p_\infty)}{0.5\rho U_m^{\,2}} \tag{3}$$

Figure 5 illustrates the effect of Reynolds numbers on the static pressure distribution versus the path distance (s/e) on square rib surface for one ribbed wall with different rib pitches. It is observed from these figures that the static pressure distribution is

independent of Reynolds numbers when Re >17,451, Re > 11,849, and Re > 11,944 for p/e = 10, 20, and 40, respectively. Also for two ribbed walls, the static pressure is independent of Reynolds numbers for two-ribbed walls when Re > 10,748 as shown in Fig. 6.

Figure 7 shows the static pressure distributions on a trapezoidal rib surface where it is independent of Reynolds numbers for two ribbed-walls when Re > 18,143, Re > 11,351, and Re > 11,933 for p/e = 10, 20, and 40, respectively. For inverted trapezoidal rib shape, the static pressure distribution is independent of Reynolds numbers as shown in Fig. 8 when Re > 11,450, Re > 11,933, and Re > 12,027 for p/e = 10, 20, and 40, respectively. It can be seen from Figs. 5-8 that the separation point of flow occurs at front sharp edge of the rib where the static pressure decreases suddenly to a minimum value at the upper face of rib. The main flow direction in all figures is from left to right and the static pressure distribution on the front face of rib is higher than that of the rear face. Downstream the separation point, the boundary layer separated from front edge of rib reattaches to the upper face of rib and the static pressure increases again to the downstream face. It is observed that the static pressure coefficients have a sharp peak at stagnation point for front face ($(2/3)e$) of rib and then decreases rapidly from stagnation point to reach a minimum value at (0.25e) downstream the separation point. Beyond the minimum value, the static pressure increases again in the farther downstream region to reach a second stagnation point on the back face and it decreases again to the corner of the back face of rib with the duct wall.

It is found that the static pressure coefficient depends on the rib alignment, it was independent of Reynolds numbers. At same rib pitch (p/e = 20) and Reynolds number (Re = 32,000), Figs. 9a-9c, illustrate the effect of rib alignment on the static pressure distributions for square, trapezoidal, and inverted trapezoidal ribs, respectively. It is observed in Figs. 9a- 9b that the static pressure for in-line alignment has lower values than those for staggered alignment and one ribbed wall alignment. This occurs because in case of in-line alignment, a higher effective blockage and distortion are found which accelerate the flow and therefore the static pressure decreases.

The variations of the static pressure coefficients versus the path distance on rib surface with different rib shapes are illustrated in Fig. 10a and Fig. 10b for one ribbed- wall and two ribbed-walls, respectively. It is observed that the static pressure has lower values for the inverted trapezoidal rib shape than the square and trapezoidal ribs.

The average static pressure coefficients ($\overline{C_p}$) on rib surface were computed by integration over rib surface and plotted against rib pitch for different rib shapes for one ribbed wall and two ribbed-walls as shown in Fig. 11a and Fig. 11b, respectively. The low values of average pressure coefficient on the inverted trapezoidal rib surface are much more likely to occur than those on the square and trapezoidal rib as shown in Figs. 11a-11b. The average static pressure coefficient increases as the rib pitch increases with different rib shapes. It is observed in Fig. 11b that the rib geometry effect on the average static pressure is more significant at low value of rib pitch (p/e=10) while as the rib pitch increases to p/e = 40, the three rib shapes approach nearly the same values of average pressure. As a result an improvement in the airflow around the inverted trapezoidal rib is observed. Therefore, the inverted trapezoidal rib accelerates and distorts the flow more than the square and trapezoidal ribs. Therefore, the heat transfer enhancement may be attained in the inverted trapezoidal rib shape employed in the present work.

Figure 12a and Fig. 12b show the variations in base pressure coefficient (Cp_b) at the rear stagnation point (s/e = 2.7) versus the rib pitch with different rib shapes for one ribbed-wall and two ribbed-walls, respectively. It is observed in Fig. 12a that the base pressure coefficient is nearly independent of the rib pitch and dependent on the rib geometry. While for the two ribbed-walls, the base pressure is dependent on the rib pitch and rib geometry for ($10 \leq p/e \leq 40$) and it increases by increasing the rib pitch. The center of the recirculation region increases as the rib pitch increases where the wake region downstream the rib becomes more stagnant.

3.1 Friction Factor

Figures 13a-13c illustrate the variation of the friction factor versus Reynolds number, for fully developed two ribbed-walls flows with square, trapezoidal, and inverted trapezoidal ribs, respectively. The results of smooth duct are also included for comparison. The friction factors decrease slowly with increasing Reynolds number and then it attains almost a constant value for $Re \geq 30{,}000$.

For a given Reynolds number, the friction factor decreases with increasing the rib pitch (p e) from 10 to 40. It is observed that there is an increase in friction factor in all cases for ribbed-walls compared with the case of the smooth duct.

Friction factor for fully developed ribbed-walls flows versus Reynolds number with different types of rib alignment for trapezoidal and inverted trapezoidal ribs are shown in

Fig. 14a and Fig. 14b, respectively. As shown in Figs. 14a-14b, the friction factors depend on the types of rib alignment and are independent of Reynolds numbers. For a given Reynolds number, the friction factor in the in-line alignment has a value higher than that in the staggered type rib alignment because of the higher effective blockage in the case of the in-line than in staggered alignment. This is may be explained in terms of the pressure drop in case of in-line alignment which is higher than that in staggered because of the blockage and distortion of the flow is more significant in case of in-line alignment generated by opposite ribs.

Friction factor for fully developed ribbed-duct flows versus Reynolds number with different rib shapes is shown in Fig. 15. It is observed that the friction factor depends on the rib geometry and is independent of Reynolds numbers. The friction factor for trapezoidal rib, square rib, and inverted trapezoidal rib are higher than those of the smooth-tube flows as given by Blasuis equation by 9-10 times, 9-11 times, and 8-11 times, respectively. Also, the results show that for two ribbed-walls with square ribs, there is a good agreement with the previous results of fully developed ribbed-duct flows reported by Liou et. al., 1992(part 1). However, the present results are higher than those of Liou et. al., 1992 (part 1) by about 9 %. This comparison is made to validate the present experimental measurements.

3.2 FLOW VISUALIZATION RESULTS

The recirculating flow with corner vortices upstream and downstream the ribs is difficult to be measured but can be described by flow visualization, in terms of the reattachment length (distance from the rear face of rib to the point of flow impingement to the ribbed-wall of channel). The visualization tests were carried out for channel with two-ribbed walls (e/H = 0.125) with different rib pitches (p/e = 5, 10, 15, and 20) and shapes (square, trapezoidal, and inverted trapezoidal ribs). A uniform flow of smoke passes to the channel with two-ribbed walls with different velocities.

Figures 16a-16c show the flow patterns through channels with two-ribbed walls for different rib pitches, shapes, and types of rib alignment. For different rib pitches in Fig. 16a and when Re = 5870, it is observed that as the rib pitch increases the wake region formed downstream the ribs extended slightly. This recirculating region which has vortices with rotational flow becomes more stagnant. The shear layers separated at the front edge of rib are reattached to the ribbed-wall of channel at an impingement point at

a distance of (4.5 e) approximately downstream the rib and slightly depends on the rib pitch for p/e > 10.

It can be observed from Fig. 16b that for p/e = 5, the impingement of flow occur nearest to the downstream rib or on rib surface itself. This shows that the inter-distance between two consecutive ribs is completely occupied by the recirculating regions for p/e < 10. Also, this indicates that the downstream rib falls completely in the wake region of the upstream rib. For channel with staggered rib alignment (p/e = 20); it is observed from Fig. 16c that the flow appears more likely to reattach to the ribbed-walls and this yield good enhancement for heat transfer. The experimental correlations of the average static pressure coefficient on rib surface with different rib shapes are developed in terms of Reynolds number and rib pitch in equation (1). Also the friction factor correlations for different rib shapes are developed in equation (2).

$$\overline{C_p} = a_1 . \mathrm{Re}^{a_2} . (p/e)^{a_3} \qquad (1)$$

$$f = b_1 . \mathrm{Re}^{b_2} . (p/e)^{b_3} \qquad (2)$$

The constant coefficients a_1, a_2, a_3, b_1, b_2, and b_3 are listed in table 2. The maximum relative errors in equation (1) are ± 6 %, ± 9 %, and ± 4 % for trapezoidal, square and inverted trapezoidal ribs, respectively, and in equation (2) are ± 9 %, and ± 12 % for trapezoidal and inverted trapezoidal ribs, respectively.

TABLE 2: CONSTANT COEFFICIENTS IN EQUATION (1) AND (2)

Constant Coefficients	Rib Geometry		
	Trapezoida	Square	Inverted Trapezoidal
a_1	-4.71	-6.168	-14.38
a_2	0.013	0.03	-0.0348
a_3	-0.31	-0.422	-0.436
b_1	0.487	-	0.448
b_2	-0.101	-	-0.104
b_3	-0.488	-	-0.417

4. ANALYTICAL RESULTS

ANSYS program uses the k-ε turbulence model and solves the governing equations and the turbulence flow equations by the finite element technique. All solutions apply a uniform velocity profile at inlet and zero velocity condition in the direction normal to the

inlet flow. No-slip (zero velocity) conditions are applied all along the walls. Zero relative pressure parameters at the duct outlet. The grid elements used here are denser in the two-dimensional plane and the total number of grid elements greater than those used for the three-dimensional. The present work uses a model which has 32,650 elements that gives a reattachment length of (x_l = 4.4e) which lies in the range of Liou et. al., 1993. The numerical results of the relative velocity (u/u_∞) and pressure (p/p_d) are shown as numbers in Fig. 17. Figure 17 illustrates the velocity and pressure contours distributions around ribs mounted on the two opposite walls with different rib shapes at Re = 31,200 and p/e = 10. It is observed that, the regions upstream and downstream the ribs are two stagnation regions. The non-dimensional velocity has a higher value nearest to the separation point and at the mid-line of the ribbed-duct. It is observed that the higher values of the non-dimensional pressure occur on the front face of rib (stagnation point) at 2/3 e and the lower values on the back face. Good agreement is found between the computed pressure contours on rib surface (Fig. 17) and the experimental results for different rib shapes as shown in Fig. 10b for Re = 31,200 and p/e =10.

5. CONCLUSIONS

The experimental results for the two ribbed-walls of channel and the flow visualization show the following: -

1. The static pressure coefficient for in-line alignment of ribs has lower values than those for staggered alignment and one ribbed-wall alignment while it was independent of Reynolds numbers.
2. The static pressure coefficient has lower values for the inverted trapezoidal rib shape than square and trapezoidal ribs.
3. The average static pressure coefficient on rib surface increases as the rib pitch increases with different rib shapes.
4. The rib geometry effect on the average static pressure is more significant at low values of rib pitch (p/e=10) while as the rib pitch increases to p/e = 40, the three rib shapes approach nearly the same values of average pressure.
5. The base pressure coefficient is dependent on the rib pitch and rib geometry for ($10 \leq p/e \leq 40$) where it increases by increasing the rib pitch.
6. The friction factors decrease slowly with increasing Reynolds number and then it attains a constant value approximately for Re $\geq$ 30,000.

7. For a given Reynolds number, the friction factor decreases with increasing the rib pitch (p/e) from 10 to 40.
8. The friction factor in the in-line rib alignment has a value higher than that in the staggered type rib alignment because of the higher effective blockage in the case of the in-line than in staggered alignment.
9. The friction factor for trapezoidal rib, square rib, and inverted trapezoidal rib are higher than the results of the smooth-tube flows from Blasuis equation by 9-10 times, 9-11 times, and 8-11 times, respectively.
10. There is a good agreement for the friction factor measurements with the previous results of fully developed ribbed-duct flows with square ribs reported by Liou et. al., 1992 (part 1) where the present results are higher than Liou et. al., 1992 (part 1) by about 9 %.
11. It is observed from flow visualization that, as the rib pitch increases the wake region downstream the ribs extended slightly and this recirculating region which has vortices with rotational flow becomes more stagnant.
12. The wake region formation around the leading rib of ribbed-channel becomes much more than the downstream ribs where the boundary layer breaks up in flow direction.
13. The inter-distance between two consecutive ribs is completely occupied by the recirculating regions for p/e < 10. This indicates that the downstream rib falls completely in the wake region of the upstream rib.
14. The theoretical results are in a good agreement with the experimental results and flow visualization results where good predictions for the separation point and reattachment point.

NOMENCLATURE

a.	- rib width	m
C_p	-static pressure coefficient, $C_p = \frac{(p_s - p_\infty)}{0.5\rho u_m^2}$	
C_{p_b}	-base pressure coefficient, $C_{p_b} = \frac{(p_b - p_\infty)}{0.5\rho u_m^2}$	
$\overline{C_p}$	-average static pressure coefficient on rib surface	
De	-hydraulic diameter	m
e.	-rib height	m
f	-average friction factor	
H	-channel height	m
p.	-rib pitch	m
p_s	-static pressure	Pa

p_b	-base pressure	Pa
p_∞	-static pressure at (29 e) upstream the ribbed-duct	Pa
p_d	- dynamic pressure, $(0.5\rho u_m)$	Pa
Δp	- pressure drop across the flow channel	Pa
Re	-Reynolds number, (ρuDe/μ)	
s.	-path distance on rib surface	m
u	-axial velocity in x-direction	m/s
u_m	-axial mean velocity upstream the ribbed-duct	m/s
U_m	-mean velocity at entrance to the main duct	m/s
x	-streamwise coordinate	m
x_l	-reattachment length	m
Δx	- axial distance	m
y	-transverse coordinate	m
z	-spanwise coordinate	m

Greek Symbols

θ	-angle intercept between the front face of rib and channel wall	deg.
μ	-dynamic viscosity	kg/m.s
ρ	-density	kg/m^3

Subscripts

d.	-dynamic
s	-static
o	-smooth
∞	-inlet
l	- impingement point

Abbreviations

AC	-Alternating Current
CFD	-Computational Fluid Dynamics
LDV	-Laser-Doppler Velocimeter

REFERENCES

ANSYS, "CFD FLOTRAN Analysis Guide," ANSYS, Inc., 1997.

Han, J.C., "Heat Transfer and Friction Characteristics in Rectangular Channels With Rib Turbulators," ASME Journal of Heat Transfer, Vol. 110, No. 2, pp. 321-328, 1988.

Hong, Y. J. and Hsieh, S. S., "Heat Transfer and Friction Factor Measurements in Ducts With Staggered and in-Line Ribs," Transactions of the ASME, Vol. 115, February 1993.

Han, J. C., Zhang, Y. M., and Lee, C. P., "Augmented Heat Transfer in Square Channels With Parallel, Crossed, and V-Shaped Angled Ribs," Transactions of the ASME, August, Vol. 113, PP. 590-596, 1991.

Han, J.C., "Heat Transfer and Friction in Channels With Two Opposite Rib-Roughened Walls," Transactions of the ASME, Vol. 106, pp. 774-781, 1984.

Liou, T. M. and Hwang, J. J., "Turbulent Heat Transfer augmentation and Friction in Periodic Fully Developed Channel Flows," Transactions of the ASME, Vol. 114, pp. 56-64, February 1992, (part 2).

Liou, T. M. and Hwang, J. J., "Effect of Ridge Shapes on Turbulent Heat Transfer and Friction in a Rectangular Channel," Int. J. Heat Mass Transfer, Vol. 36, No. 4, pp. 931-940, 1992, (part 1).
Liou, T. M., Hwang, J. J., and Chen, S. H., "Simulation and measurement of enhanced turbulent heat transfer in a channel with periodic ribs on one principal wall," Int. J. Heat Transfer, Vol. 36, No. 2, pp. 507-517, 1993.
Liou, T. M., Wu Y. Y., and Chang Y., "LDV Measurements of Periodic Fully Developed Main and Secondary Flows in a Channel With Rib-Disturbed Walls," Journal of Fluids Engineering, March 1993, Vol. 115, pp. 109-114, 1993.
Liou, T. M. and Chen, S. H., "Turbulent heat and fluid flow in a passage disturbed by detached perforated ribs of different heights," Int. J. Heat Mass Transfer, Vol. 41, No. 12, pp. 1795-1806, 1998.

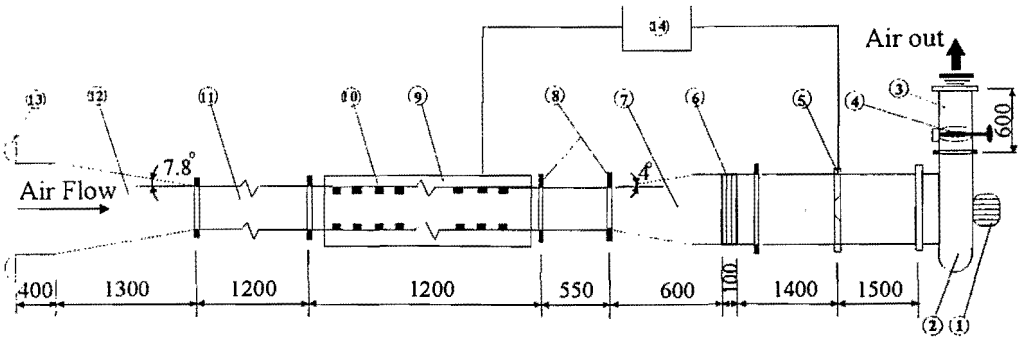

1. AC electric motor.
2. Air blower.
3 Exit duct.
4. Air gate controller.
5. Flow orifice meter.
6. Straightener.
7. Transformation duct.
8. Flanges.
9. Test section.
10. Ribs.
11. Main duct.
12. Contraction duct (10:1).
13. Bell-mouth intake.
14. Micromanometer.

Fig.1. Schematic Diagram of The Test Rig.

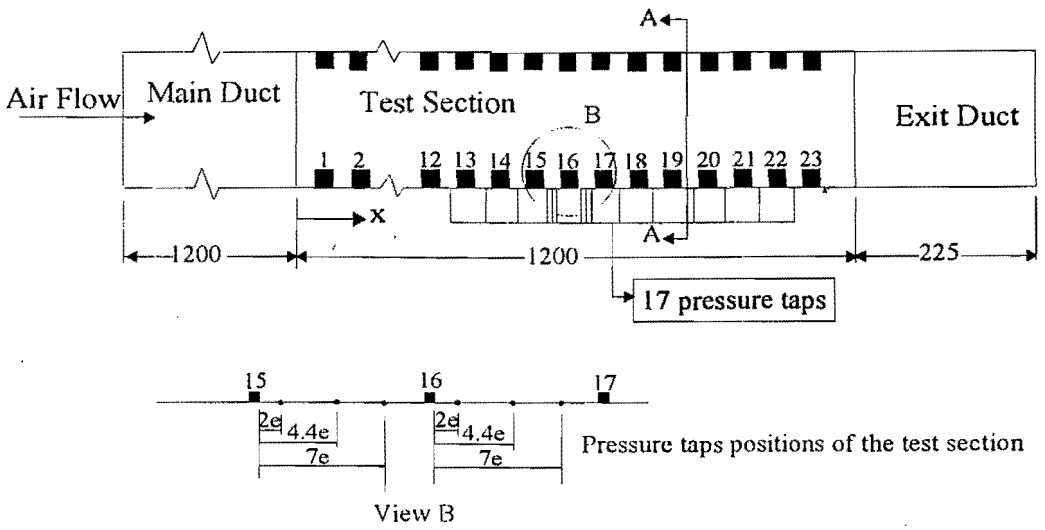

Fig.2. Test Section Details

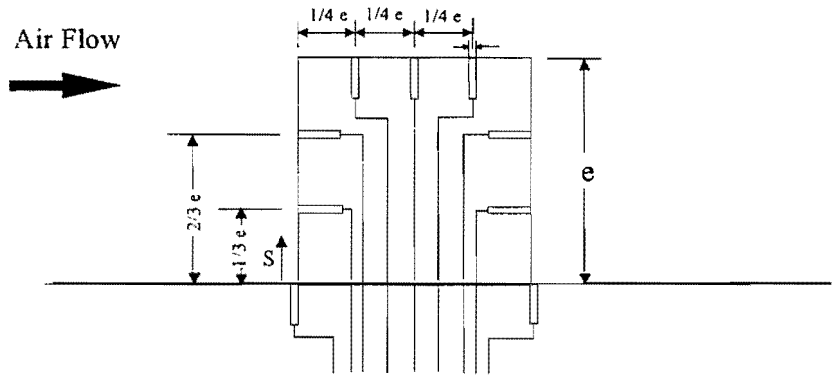

Fig.3. Details of Pressure Taps Distribution on Rib Surface.

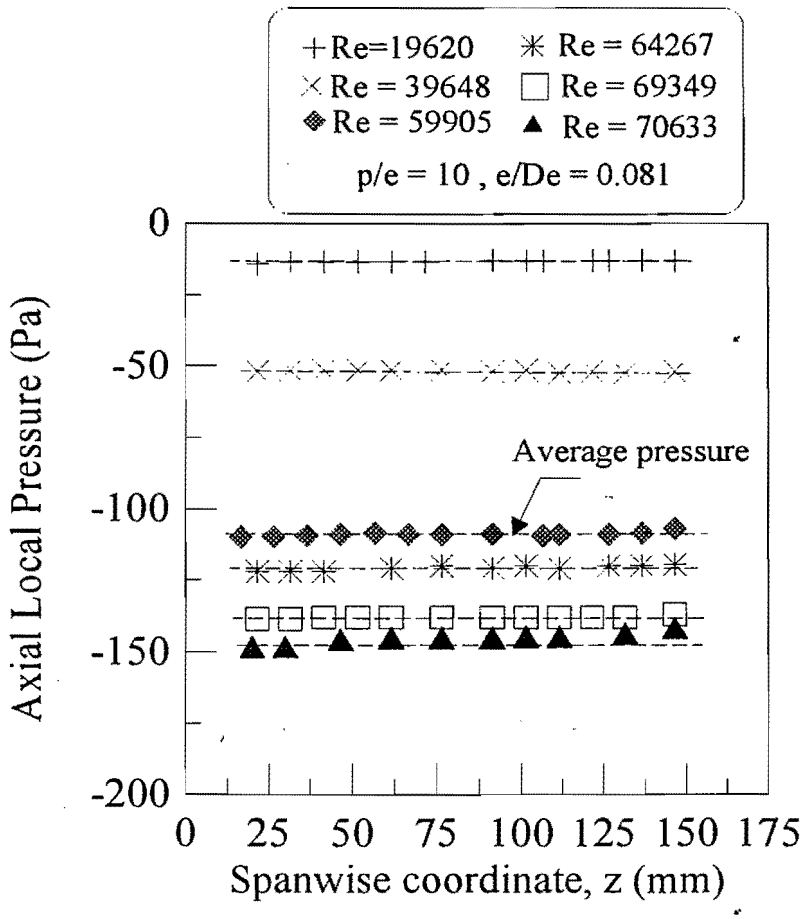

Fig.4. Spanwise Distribution of Axial Local Pressure at Various Reynolds Numbers.

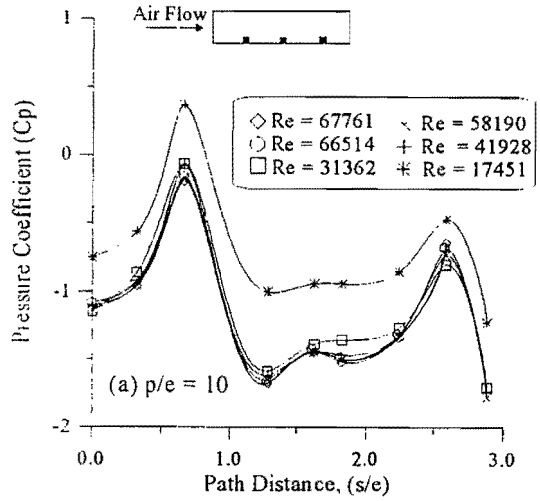

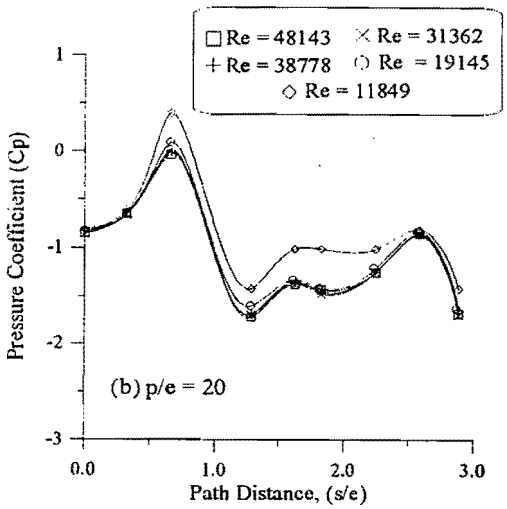

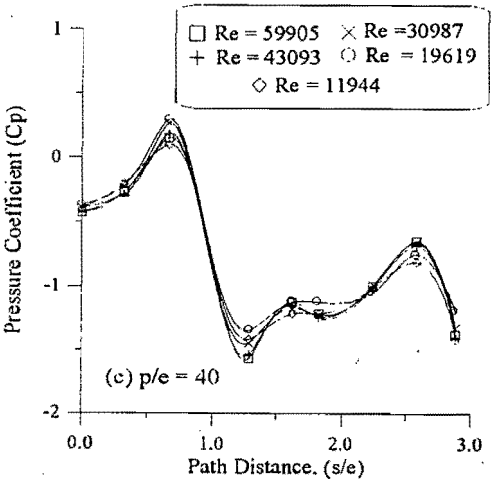

Fig.5. Variation of Local Static Pressure Coefficient Versus The Path Distance on Square Different Rib Pitches For One Ribbed-Wall

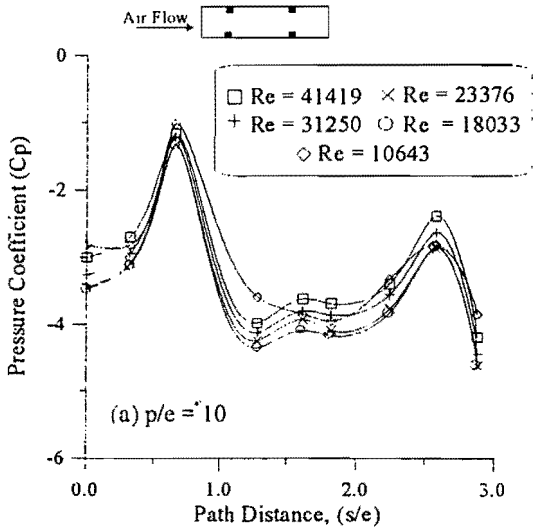

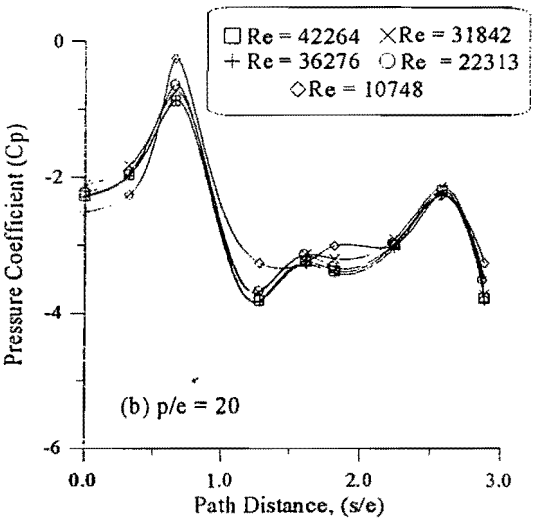

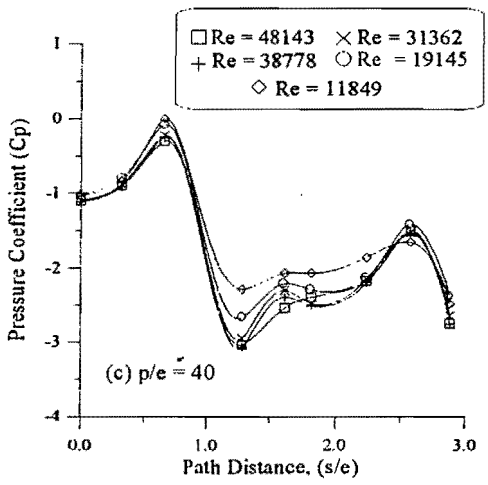

Fig.6. Variation of Local Static Pressure Coefficient Versus The Path Distance on Square Rib surface for Two-Walls With Different Rib Pitches for In-Line Rib-Alignment

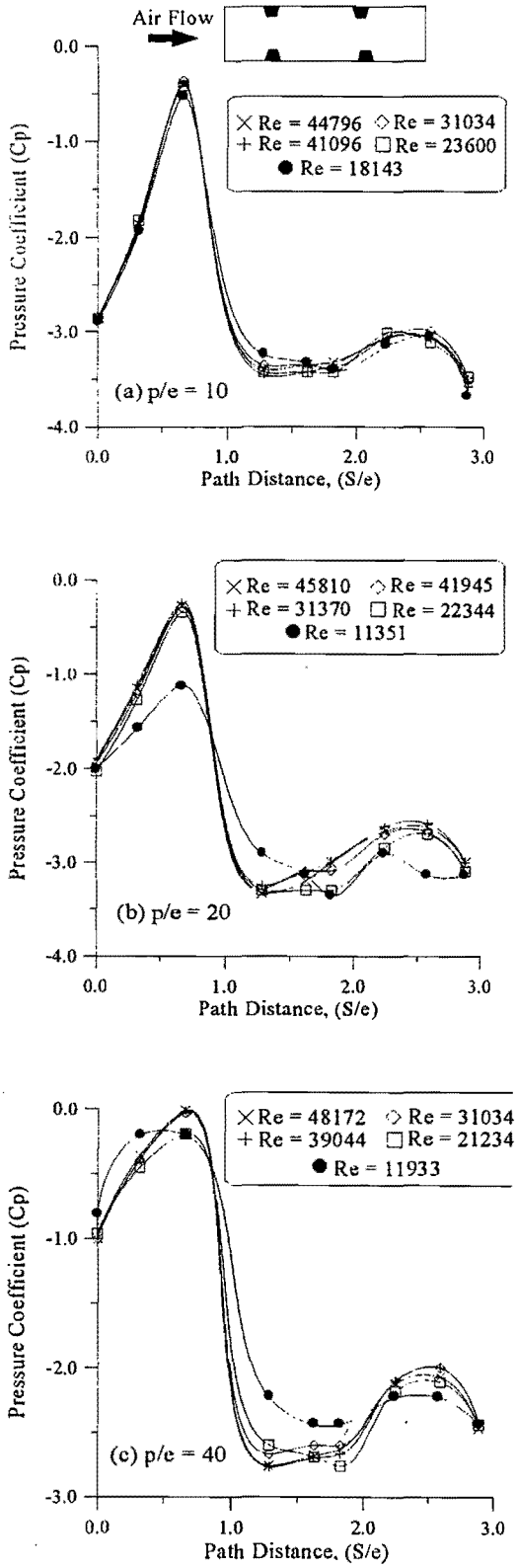

Fig.7. Variation of Local Static Pressure Coefficient Versus The Path Distance on Trapezoidal rib With Different Rib Pitches For two-Ribbed walls

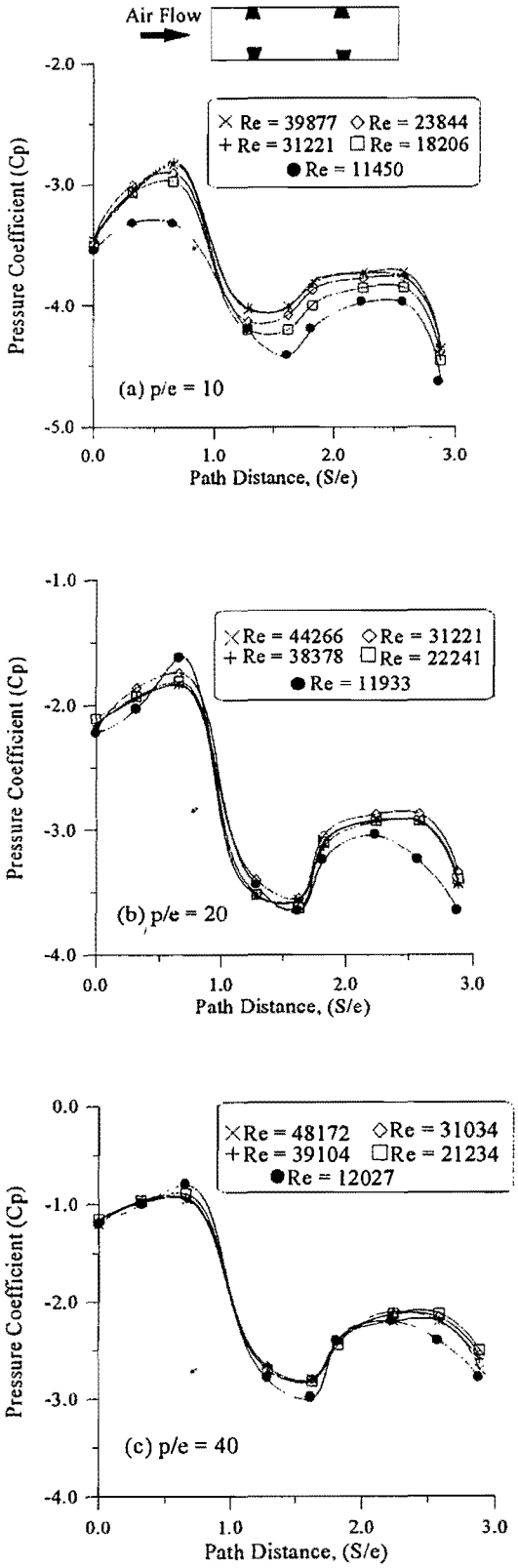

Fig.8. Variation of Local Static Pressure Coefficient Versus The Path Distance on Inverted Trapezoidal Rib With Different Rib Pitches For Two-ribbed walls

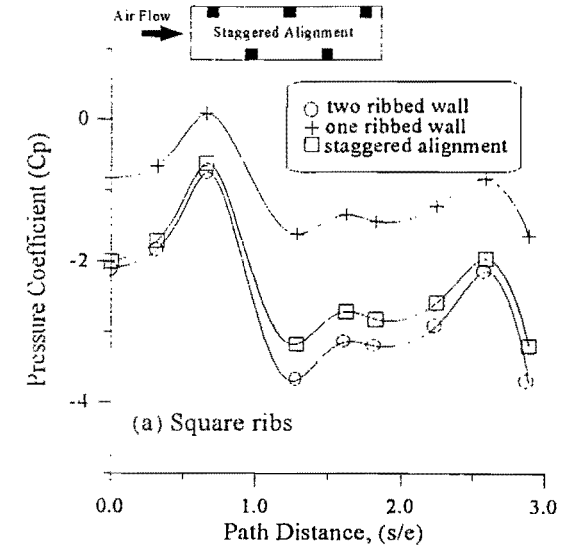

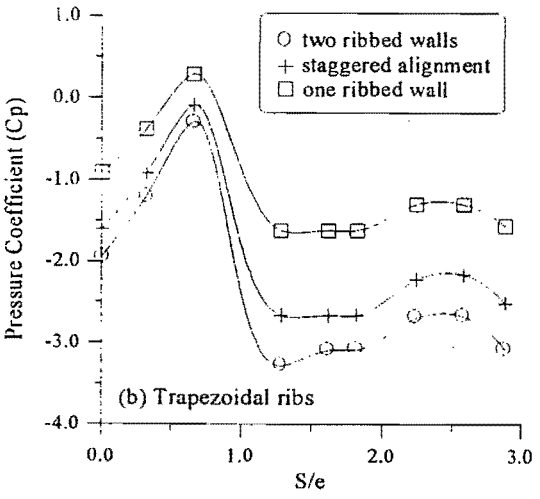

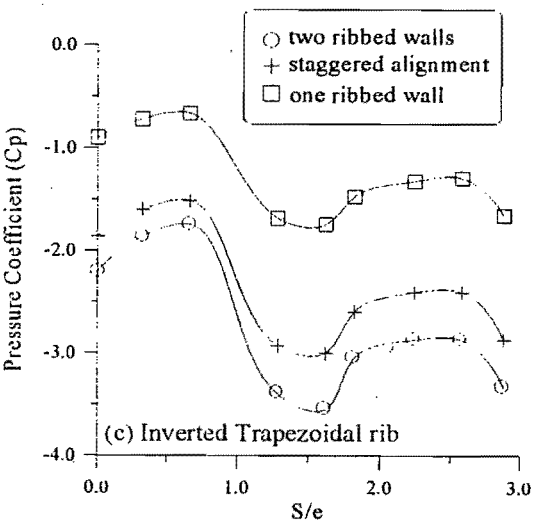

Fig.9. Comparison Between The Local Static Pressure Coefficients With Different Rib Shapes at Different Types of Rib Alignment (p/e = 20, Re = 32,000)

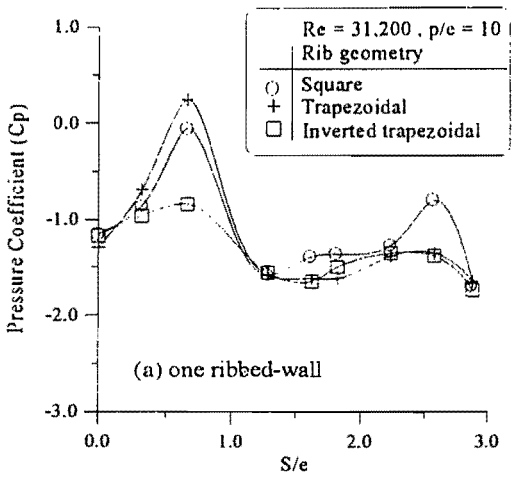

Fig.10a. Comparison Between The Local Static Pressure Coefficient With Different Rib Shapes For One Ribbed-wall

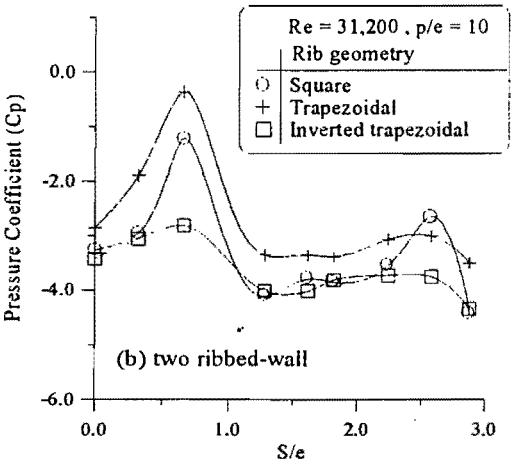

Fig.10b. Comparison Between The Local Static Pressure Coefficient With Different Rib Shapes For Two-Ribbed walls

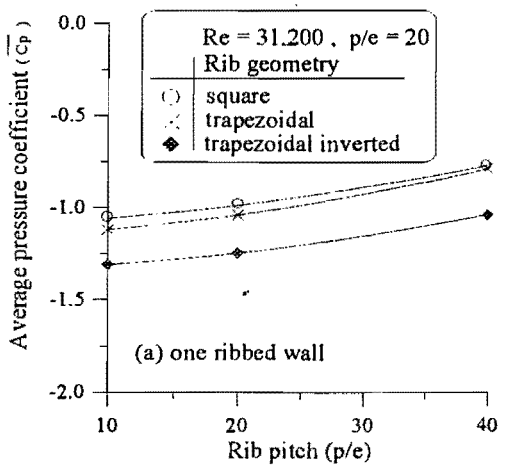

Fig.11a. Average Static Pressure Coefficient Variations Versus The Rib Pitches With Different Rib Shapes For One Ribbed-Wall

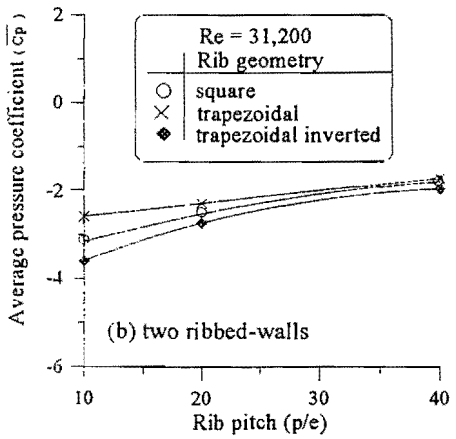

Fig.11b. Average Static Pressure Coefficient Variations Versus The Rib Pitch With Different Rib Shapes For Two Ribbed-walls

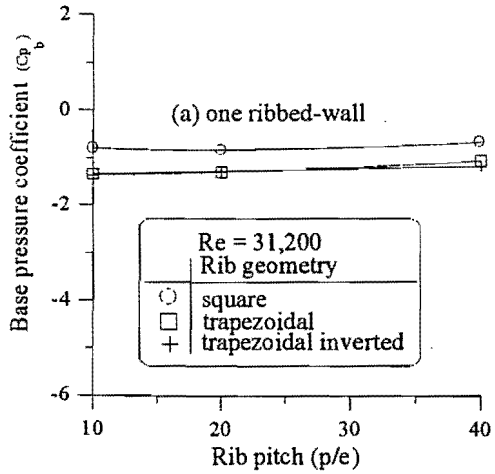

Fig.12a. Base Pressure Variations Versus The Rib Pitch With Different Rib Shapes For One Ribbed-Wall

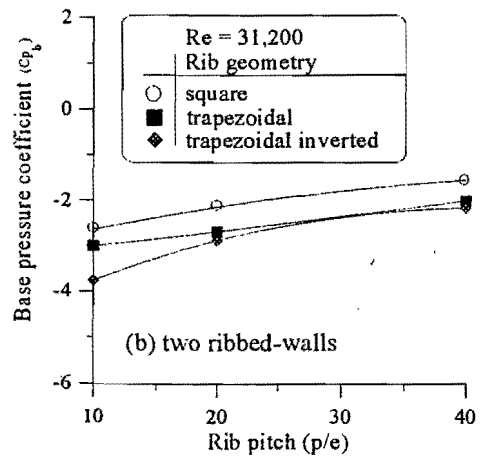

Fig.12b. Base Pressure Variations Versus The Rib Pitch With Different Rib Shapes For Two Ribbed-Walls

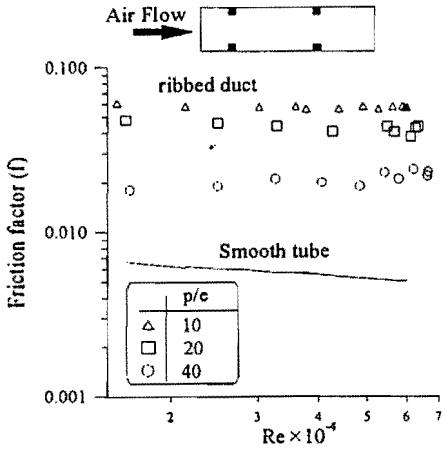

Fig.13a. Fully Developed Friction Factor Versus Reynolds Numbers For Square Ribs With Different Rib Pitches

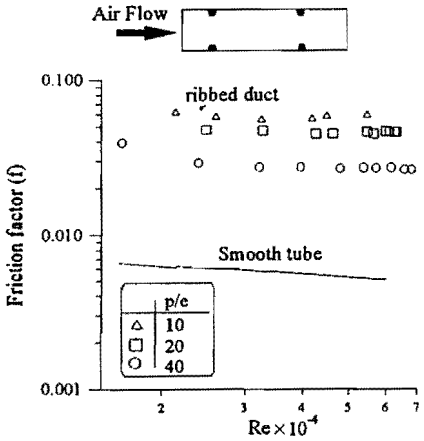

Fig.13b. Fully developed Friction Factor Versus Reynolds Numbers For Trapezoidal Ribs With Different Rib Pitches

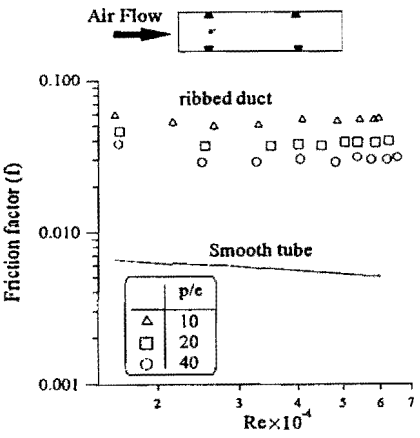

Fig.13c. Fully Developed Friction Factor Versus Reynolds Numbers For Inverted Trapezoidal Ribs With Different Rib Pitches

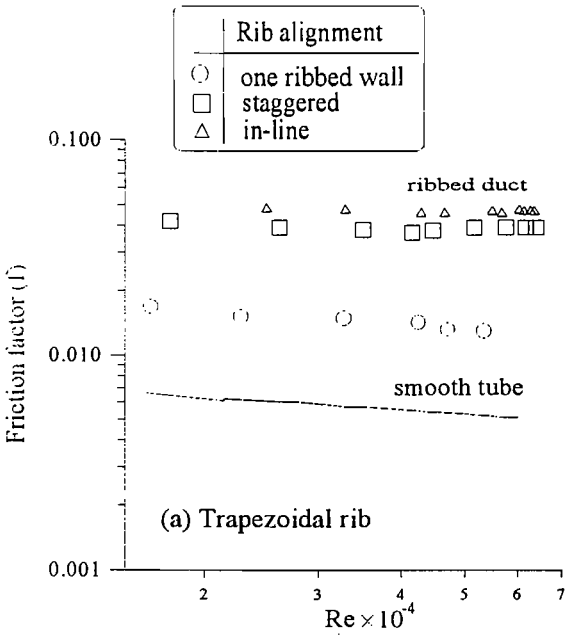

Fig.14a. Fully Developed Friction Factor Versus Reynolds Numbers For Trapezoidal Rib With Different Types of Rib Alignment (Re = 31,200, P/e = 20)

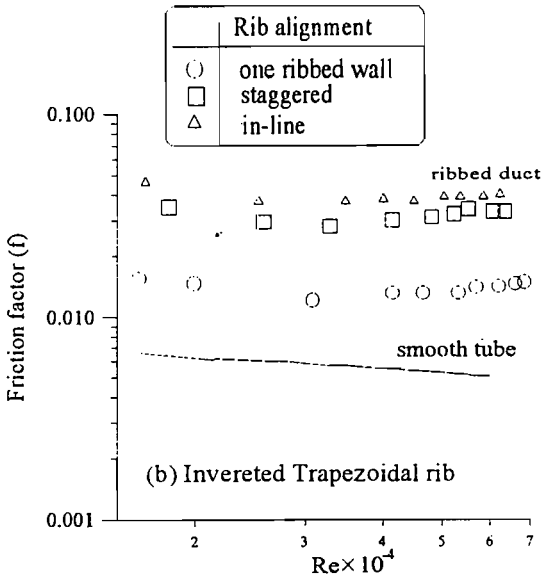

Fig.14b. Fully Developed Friction Factor Versus Reynolds Numbers For Inverted Trapezoidal Rib With Different Types of Rib Alignment

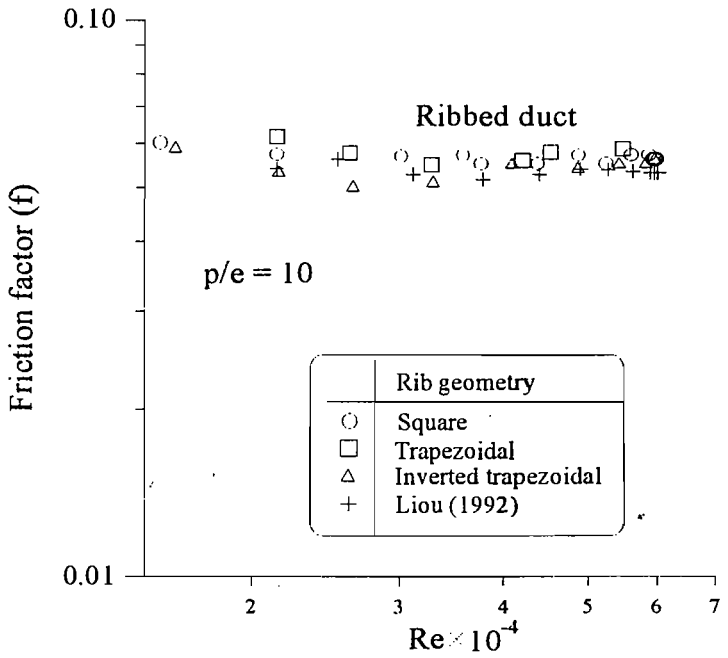

Fig.15. Fully Developed Friction Factor Versus Reynolds Number For Two Ribbed-Walls With Different Rib Shapes

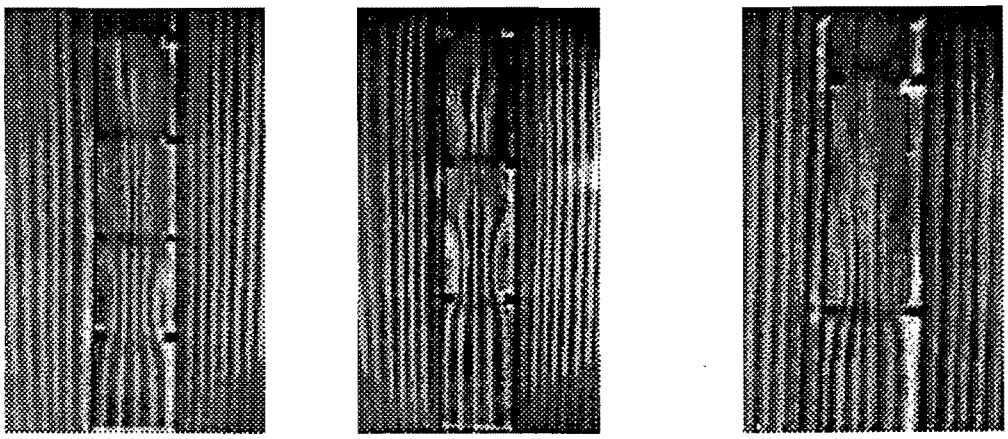

p/e = 10 p/e = 15 p/e = 20

(a) Square Ribs

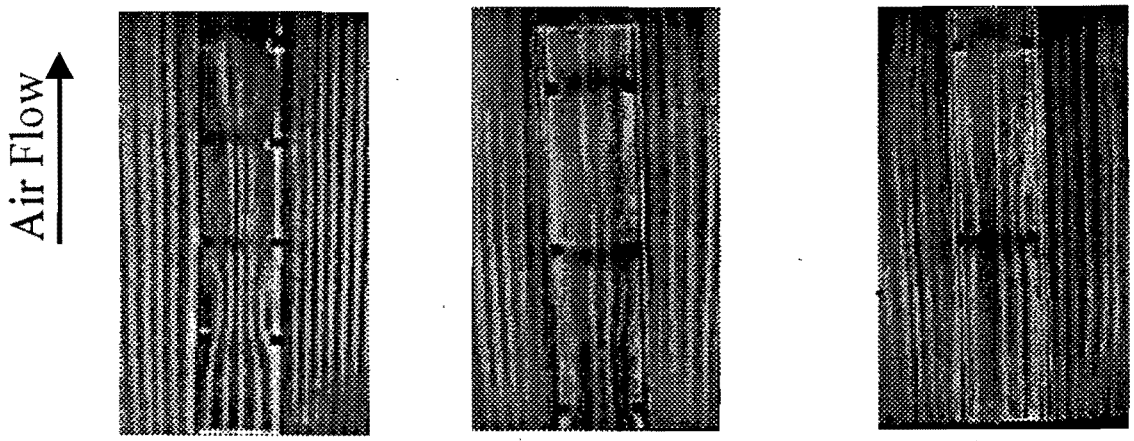

p/e = 10 p/e = 15 p/e = 20

(b) Trapezoidal Ribs

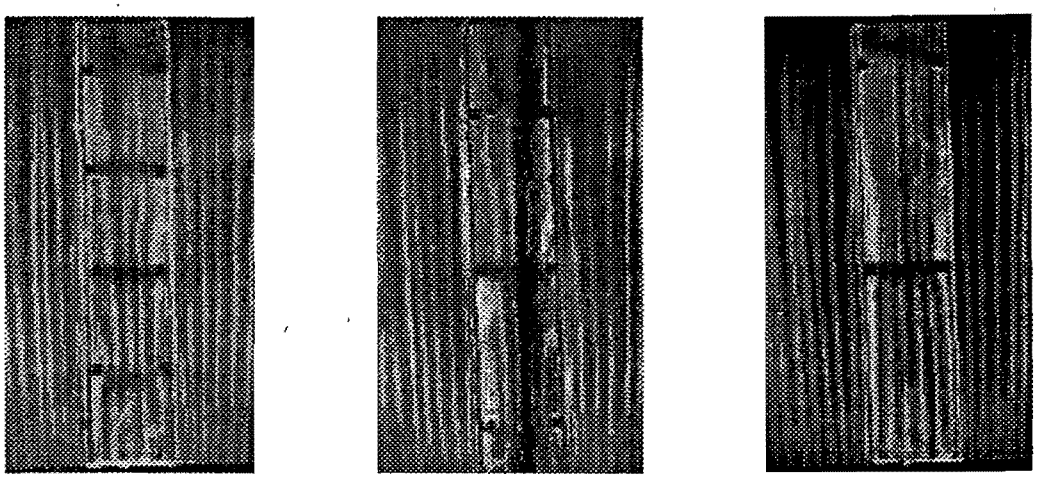

p/e = 10 p/e = 15 p/e = 20

(c) Inverted Trapezoidal Ribs

Fig.16a. Flow Visualization Through Two Ribbed-Walls For Different Rib Pitches (e/H = 0.125, Re = 5870), (Front View)

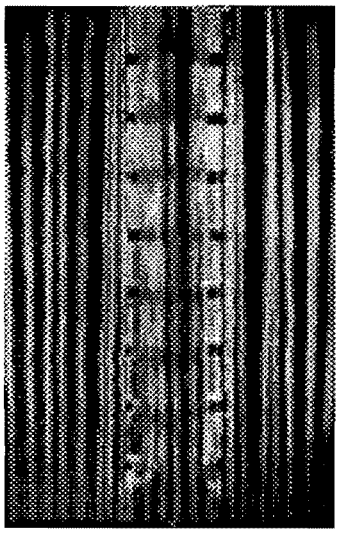

Fig.16b. Flow Visualization Through Two Ribbed-Walls With Square Ribs (p/e = 5)

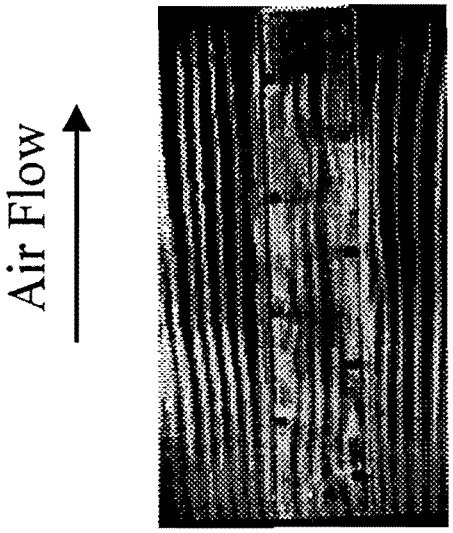

Fig.16c. Flow Visualization For Staggered Alignment of Square Ribs (p/e = 20)

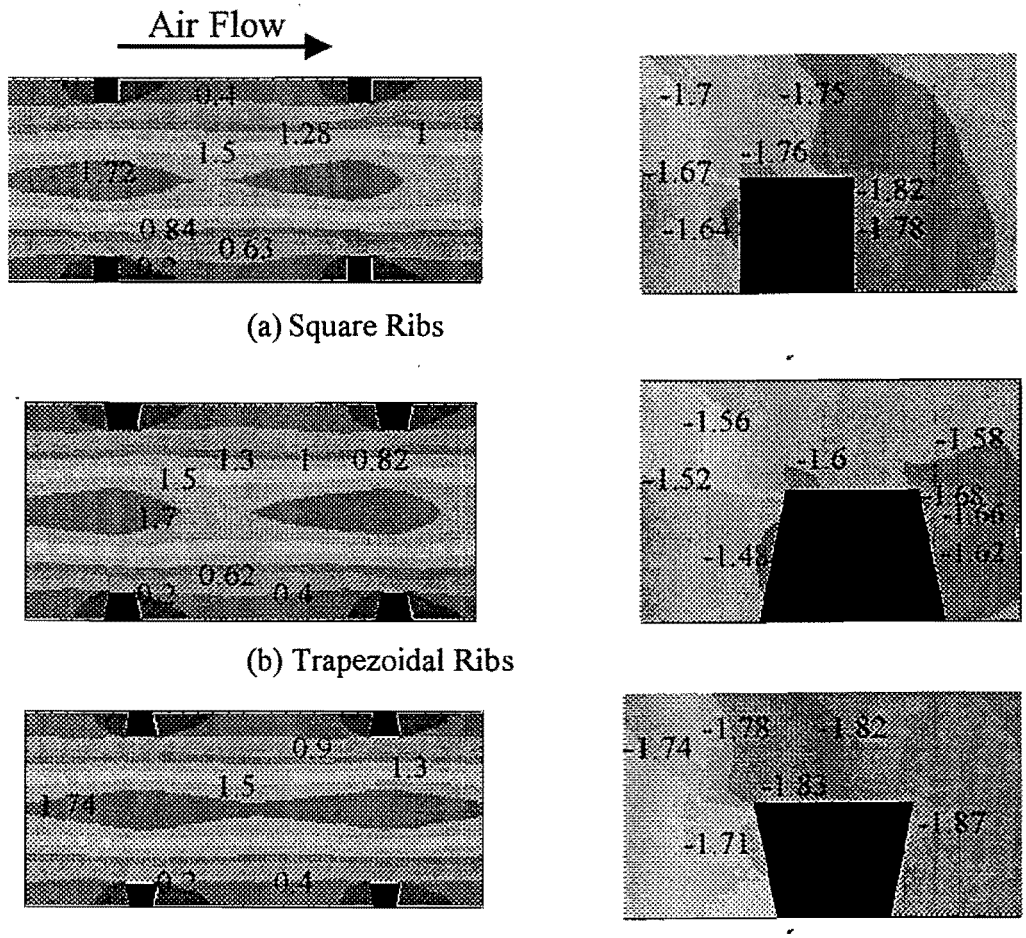

Fig.17. Velocity and Static Pressure Coefficient Contour Distributions Around Ribs of Two Ribbed-Walls of Channel With Different Rib Shapes, Using ANSYS Code (p/e = 10, Re = 31,200, e/De = 0.081)